Journal of Applied Fluid Mechanics, Vol. 17, No. 1, pp. 1-18, 2024.
Available online at www.jafmonline.net, ISSN 1735-3572, EISSN 1735-3645.
https://doi.org/10.47176/jafm.17.1.2157

A Comparative Study of Two Numerical Methods Applied for 3D Liquid-Liquid Taylor Flow in a Microchannel

M. Said[1†], N. Nait Bouda[1] and S. Harmand[2]

[1] *University of Science and Technology Houari Boumediene (USTHB), P56J+GMH, Bab Ezzouar 16111, Algiers, Algeria*
[2] *Polytechnic University of Hauts-de-France (UPHF), Campus Mont Houy 59313, Valenciennes, France*

†*Corresponding Author Email: medsaid@usthb.dz*

ABSTRACT

The laminar nature of flow in mini and microchannels has pushed researchers to develop novel solutions to overcome reaction rate reduction and heat/mass transfer issues. In this regard, Taylor flow is one of the possible solutions that could be used to enhance mixing inside mini and microchannels with reasonable pressure drop. The hydrodynamics of Taylor liquid-liquid flow is numerically studied in this work by employing two different droplet generation methods, specifically T-junction and patching methods. To this end, a three-dimensional model of rectangular microchannel flow is considered. The computational domain was designed and meshed by ICEM CFD and then simulated with commercial software ANSYS Fluent. The interface between the two phases was captured using the Volume of Fluid (VOF) method. The generating and development process of water droplets dispersed in an ethylene/propylene glycol carrier phase for both methods is discussed in detail. According to the results, both methods show satisfactory performance regarding liquid film and droplet shape, with only a slight difference. However, the patching method was found to be more economical in terms of computational time. This study would improve the state of knowledge on two-phase flow simulation in microchannels and thus contribute to the understanding of Taylor flow hydrodynamics.

Article History

Received July 11, 2023
Revised September 3, 2023
Accepted September 12, 2023
Available online November 1, 2023

Keywords:

CFD
Film thickness
Taylor flow
T-junction
Two-phase flow

1. INTRODUCTION

Over the past decades, microfluidic applications have attracted considerable interest in various fields, such as microelectromechanical systems (MEMS), laboratory-on-a-chip (LOC), medical and genetic engineering, chemical process engineering, and electronic cooling.

Despite the advantages it offers (e.g. high surface-to-volume ratio and precise flow control), researchers found that laminar flow inside mini and microchannels presents a major issue, requiring them to find new solutions to overcome this issue and, consequently, improve heat/mass transfer and reaction rates.

Among the various solutions proposed, two-phase flows in microchannels, in particular, the slug flow, which is also called segmented flow or Taylor flow, has shown to be effective in overcoming several difficulties faced by conventional single-phase microfluidics.

In general, two methods are used to create Taylor flows in mini and microchannels, passive and active. Passive methods are more economical, easier to implement, and generate droplets without external actuation contrary to active methods. T-Junction is one of the most common passive methods of droplet generation, used for the first time by Thorsen et al. (Thorsen et al., 2001) to generate oil droplets in water.

Earlier, numerical simulations involving two-phase flows in microchannels were not widely used compared to experimental studies. This is mainly due to the three-dimensional nature of the flow and the interface between the two fluids, and therefore leading to a high computational cost. However, the rapid development and diversity of interface tracking methods such as Volume of Fluid (VOF) (Qian et al., 2019), Lattice Boltzmann (Ba et al., 2015), Level set (Wong et al., 2017) and finally Coupled Level set and Volume of Fluid (CLSVOF) (Chakraborty et al., 2019), as well as the development of computational equipment has facilitated the task and thus encouraged numerical simulations in the field of droplet-based microfluidics (Gupta et al., 2009; Talimi et al., 2012).

An analysis and observation of the effect of grid size on slug flow simulations was conducted by Gupta et al. (2009) using computational fluid dynamics (CFD).

NOMENCLATURE

W	Channel width	Re_{TP}	Reynolds number of two phase flow ($\mathrm{Re_{TP}} = \rho_{TP} U_{TP} D_h / \mu_{TP}$)
h	Channel height	λ	Viscosity ratio($\lambda = \mu_d / \mu_c$)
D_h	Hydraulic diameter	**Greek symbols**	
L_e	Length of flow development (patching method)	δ	Film thickness
A	Cross-section area	ρ	Density
U	Velocity	μ	Viscosity
u	Longitudinal velocity (or x-velocity component)	σ	Interfacial tension
Q	Flow rate	**Subscripts**	
q	Flow rate ratio($q = Q_d / Q_c$)	c	Continuous phase
Ca_{TP}	Capillary number of two-phase flow ($\mathrm{Ca_{TP}} = \mu_c U_{TP} / \sigma$)	d	Dispersed phase
Ca_c	Capillary number of continuous phase ($\mathrm{Ca_c} = \mu_c U_c / \sigma$)	TP	Tow-phase
Ca_D	Capillary number based on plug velocity ($\mathrm{Ca_D} = \mu_c U_D / \sigma$)	D	droplet
Re_c	Reynolds number of the continuous phase ($\mathrm{Re_c} = \rho_c U_c D_h / \mu_c$)	f	film
Re_d	Reynolds number of the continuous phase ($\mathrm{Re_d} = \rho_d U_d D_h / \mu_d$)	Cr	Corner

Various grid sizes were tested, ranging from D/20 to D/100 elements. However, physical results could only be obtained when the mesh was refined to D/200. A basic strategy was suggested by the researchers which consisted of refining the mesh in the radial direction near the channel wall with a minimum of five elements to keep the interface sharp near the liquid film. As a result, their simulations were extremely computationally expensive.

Navaneetha et al. (2010) conducted a numerical simulation to determine the effect of the momentum discretisation scheme and the gradient calculation scheme on the simulation of two-phase flow. The volume of fluid (VOF) together with the continuum surface model (CSF) are used to track the interface and incorporate the surface tension force. For the discretization of momentum, the results indicate that first order schemes (first order upwind schemes, power law) perform better than second order schemes (second order upwind schemes, QUICK), while for gradient calculation schemes, node-based schemes perform more efficiently than cell-based schemes.

Kashid and Renken (2010) developed a numerical model based on the volume of fluid (VOF) method, which was used as an interface tracking method. This model is a two-dimensional T-junction validated using experimental results of Tice et al. (Tice et al., 2004). The results showed that the VOF method describes very well the generation of plug flow and its key features such as wall film and wetting behaviour.

Using ANSYS Fluent, Asadolahi et al. (Asadolahi et al., 2011) simulate Taylor flow in a microchannel using two CFD methodologies. In the first approach, bubbles and droplets are generated in a long tube in a stationary frame (laboratory frame) of reference. In this approach, bubbles/droplets of desired size can be generated by controlling both phases' inlet flow rates. As opposed to the first approach, the second approach solves the flow in a unit cell containing one liquid slug and half a bubble on each side of the slug in a frame of reference moving with the bubble velocity. The results show that moving domain approaches require considerably less computational power than stationary domain approaches. However, both approaches produce the same results, giving confidence in their implementation.

Motivated by the lack of studies that examined the effect of viscosity ratio on droplet size, Nekouei et al. (2017), using the Volume of Fluid method (VOF), conducted three-dimensional numerical simulations of droplet formation in T-junction microfluidic devices. The authors employed a rectangular microchannel with a viscosity ratio between 0.01 and 15. According to the findings, droplet size decreases with increasing Ca number for all viscosity ratios λ. However, the researchers pointed out that this reduction in droplet size was more pronounced for $\lambda<1$ than for $\lambda>1$. They also mapped the dependence of droplet volume on the viscosity ratio ($0.01 < \lambda < 15$) and the Ca number ($0.001 < Ca < 0.5$). The droplet formation mechanism was also investigated by measuring filling and squeezing times for different Ca and viscosity ratios. For a fixed Ca number, the researchers reported that the filling stage duration for the entire viscosity ratio interval was the same, whereas for the squeezing stage duration, changing the viscosity ratio will affect the squeezing time. On the other hand, for a fixed viscosity ratio, varying the Ca number was reported to affect the filling and squeezing times.

Qin et al. (2018) were among the first researchers to use the two-dimensional patching method to generate a CO2 droplet dispersed in water. In their paper, the authors described the droplet generation process using this method, which consisted of two essential stages. The first stage involved droplet preparation and development, while the second was the stabilization stage. The researchers found that the final CO2 droplet length was greater than the initial droplet length (initial patch). The expansion of the initial droplet was attributed to the effects of interfacial tension and the pressure difference across the interface. Despite the interesting results presented by the

researchers, they pointed out some limitations of this numerical method, notably the lack of validation of the numerical results and the absence of a droplet generation geometry (e.g. a T-junction).

Bordbar et al. (2020) numerically examined the thermal performance of microchannel heat sinks using the patch method as one of the CFD methods. The study was performed in 3D, with two oil patches placed at the microchannel inlet as initial oil plugs and dispersed in a water carrier phase. Note that the researchers did not validate the results obtained with the patching method. However, they did validate the Volume of Fluid (VOF) method with numerical and experimental data and demonstrating its ability to capture and track the interface separating the two fluids.

Silva et al. (Silva et al., 2020) compared two simulation software packages, namely OpenFOAM and ANSYS Fluent. The objective was to investigate the ability of these two software packages to accurately predict Taylor gas-liquid flow hydrodynamics in microchannels using interface tracking methods. The Volume of Fluid (VOF) method with piewise Linear Interface Computation (PLIC) were used for the ANSYS software, while the MULES and isoAdvector methods were chosen for the OpenFOAM software. The results indicate that for high Ca_B (Based on bubble velocity), each software correctly predicts the main flow characteristics. However, for low capillary numbers ($Ca_B < 0.03$), spurious currents start to appear in the near-interface region resolved by the OpenFOAM software. Therefore, the researchers suggest the use of the VOF+PLIC method as a successful option for solving Taylor flow hydrodynamics at microscale.

Other attempts have been made by researchers to reduce the computational time required for two-phase flow simulations in micro scales, particularly in computational domain meshing techniques. A dynamic mesh adaptation method with interface tracking has been used by several researchers (Mehdizadeh et al., 2011; Azarmanesh & Farhadi, 2016; Bordbar et al., 2020). In this method, the basic mesh is refined based on the volume fraction gradient at the interface. This allows the reduction of nodes in the computational domain and, consequently, reduces computational time.

Bayareh et al. (2020) were not satisfied with the dynamic mesh adaptation technique based on fractional volume gradients in terms of computational time. They proposed a boundary mesh adaptation that allows refinement of the mesh size in the vicinity of the selected boundary zones. Consequently, the computational time was about one-tenth that of the uniform fine mesh with the same quality of results (Zhou & Ai, 2013).

Several previous studies that adopted the Patching method have not validated its performance against experimental results in the literature. Therefore, this present work aims to improve the state of knowledge on the simulation of two-phase flow in microchannels. It's a comparative numerical study of the hydrodynamics of liquid-liquid Taylor flow in a 3D microchannel. Two different droplet generation methods, namely the *T-junction* method and the *patching* method were tested. The Patching method will be validated by comparing the liquid film results with the experimental correlations reported previously. We have focussed our analysis on the droplet formation mechanism, liquid film thickness, the plug shape, and flow structure. Additionally, for the T-junction method, the filling time ($t_{Filling}$) and squeezing time ($t_{Squeezing}$) during the droplet formation mechanism have not been studied previously in the literature for viscosity ratios lower than 0.1 (λ<0.1). Consequently, $t_{Filling}$ and $t_{squeezing}$ is investigated as a function of viscosity ratio λ, flow rate ratio q, and capillary number Ca_{TP} (based on the mixture velocity).

2. METHODOLOGY

In this work, the ANSYS Fluent software was used for both methods. The hydrodynamics of the Taylor liquid-liquid flow in a 3D rectangular microchannel with a cross section of 600 µm × 300 µm was studied. The Taylor flow characteristics (liquid film, plug shape, pressure drop) were analysed for two combinations of the working fluids. We have selected the ethylene glycol and propylene as carrier phases "continuous phase" and water as the dispersed phase in the two cases (see Table 1). Finally, to track the interface temporally and spatially, we have employed the Volume of Fluid (VOF) method together with the geometric reconstruction algorithm.

2.1 Geometrical Model and Boundary Conditions

The numerical model consists of two geometries. The first is a three-dimensional T-junction with a cross-section of 600 µm × 300 µm and symmetry in the xy plane (Fig. 1). Uniform velocity profile was set at the continuous and dispersed phase inlets. At the outlet, a "pressure outlet" boundary condition was chosen. At the wall, a non-slip condition was imposed. Moreover, a contact angle of 180° was chosen to eliminate wettability effects.

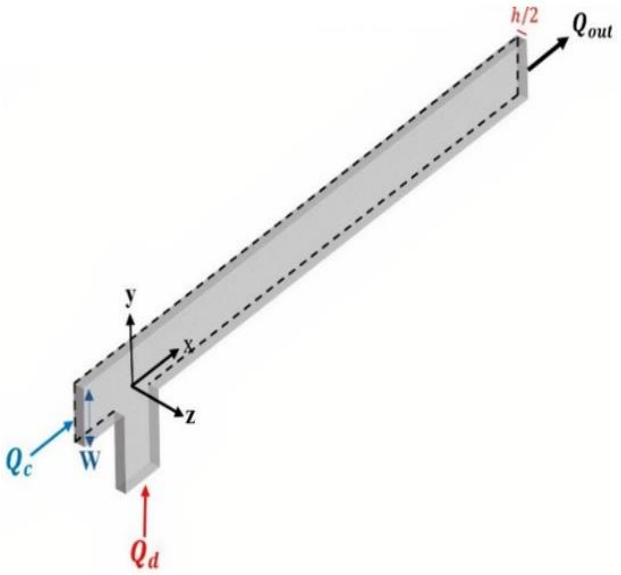

Fig. 1 Schematic design of the 3D microchannel used for the T-junction method

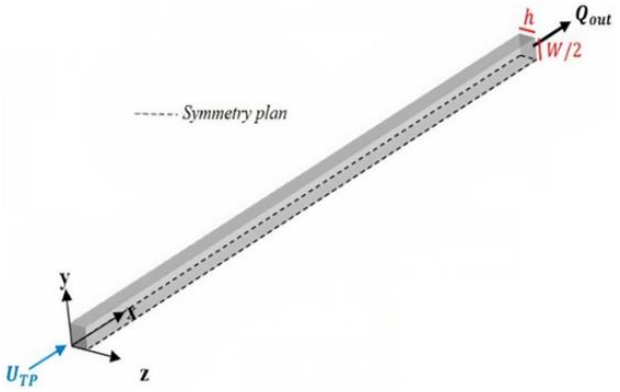

Fig. 2 Schematic design of the 3D microchannel used the Patching method

The entrance length of the channel required for the flow of each phase to fully develop before entering the junction was determined using the correlation of Dombrowski et al. (1993):

$$\frac{L_e}{D_h} = 0.379e^{(-0.148Re)} + 0.055Re + 0.26 \quad (1)$$

While the second geometry is a straight rectangular microchannel with the same cross-section. A mixture velocity is set at the microchannel inlet, with symmetry along the *xz* plane (Fig. 2). The correlation of Dombrowski et al. (1993) was also used here to estimate the flow development length before setting the dispersed phase patches.

2.2 Governing Equations

The continuity, momentum of the two-phase flow are as follows:

$$\frac{\partial \rho}{\partial t} + \nabla \cdot (\rho \vec{u}) = 0 \quad (2)$$

$$\frac{\partial (\rho \vec{u})}{\partial t} + \nabla \cdot (\rho \vec{u}\vec{u}) = -\nabla p + \nabla \cdot [\mu(\nabla \vec{u} + \nabla \vec{u}^T)] + \rho g + \vec{F} \quad (3)$$

The continuity equation for the volume fraction function φ is given by the following:

$$\frac{\partial \varphi}{\partial t} + \nabla \cdot (\vec{u}\varphi) = 0 \quad (4)$$

With φ is the volume fraction, which is zero ($\varphi = 0$) when it is in the continuous phase and one ($\varphi = 1$) when is in the dispersed phase. However, when it is between zero and one ($0 < \varphi < 1$), it signifies that we are in the interface region between the two fluids.

For a two-phase flow with Newtonian fluids and constant density ρ, the one-fluid approach was used. As a result, the physical properties (ρ, μ) are expressed as a volume-fraction weighted average.

$$\rho = \varphi_d \rho_d + (1 - \varphi_d)\rho_c \quad (5)$$

$$\mu = \varphi_d \mu_d + (1 - \varphi_d)\mu_c \quad (6)$$

The surface tension force per unit volume (F) is treated as a source term in equation (3) and calculated as indicated below:

$$F = \sigma \kappa \delta_i n \quad (7)$$

Table 1 Properties of the working fluids

/	*Continuous phase*		*Dispersed phase*
Fluids	Ethylene glycol	Propylene glycol	Water
$\rho\ (kg \cdot m^{-3})$	1109	1035	1000
$\mu\ (Pa \cdot s)$	0.01983	0.05757	0.00089
$\sigma\ (N \cdot m^{-1})$	0.048	0.0718	/

$$n = \nabla \varphi \quad (8)$$

$$\kappa = \nabla \cdot \hat{n} = \nabla \cdot \frac{n}{|n|} \quad (9)$$

$\sigma, n, \delta_i, \kappa$ are respectively the surface tension, the normal vector at the interface defined as the gradient of the volume fraction, the delta Dirac function and the curvature of the interface evaluated from the divergence of the unit normal surface $\hat{n}$.

2.3 Working Fluid

In this study, we chose ethylene and propylene glycol as the continuous phase, which perfectly wet the microchannel walls, and water as the dispersed phase with a contact angle of $\theta = 180°$ with the channel walls. Ethylene and propylene glycol were chosen based on their dynamic viscosity. The propylene glycol viscosity is about three times higher than the ethylene glycol viscosity, allowing us to examine viscosity's effect on parameters such as liquid film thickness δ and droplet shape. See Table 1 for more details.

2.4 Parameters Settings

Simulations for both droplet generation methods were conducted in ANSYS Fluent using the finite volume method. For interface reconstruction, the geometric reconstruction method was applied. The QUICK method was adopted to solve the momentum equation, while the PISO scheme was chosen to solve the pressure-velocity coupling. Green-Gauss node-based techniques were used to reduce spurious currents at the interface, whereas the PRESTO! scheme was adopted to solve the pressure equation. A variable time step was used in this study along with a fixed courant number of 0.25. For the continuity equation, the residuals were fixed at 10^{-4} to ensure accuracy, while for the other variables, the residuals were always less than 10^{-6}.

2.5 Mesh Grid Independency

Before conducting the comparative study, we performed a mesh independence study on the patching method. To this end, ICEM CFD software generates a non-uniform structured mesh with different mesh sizes. The meshes proposed here are of four different sizes: 25 µm, 17 µm, 12 µm and 7 μm. In all four cases, the mesh was refined in the wall region with a minimum of 5 to 10 nodes to capture liquid film thickness successfully. Gupta et al. (Gupta et al., 2009) suggested that a minimum of five elements is required near the channel wall to successfully capture the thin liquid film. The first cell size in the near wall zone was kept constant for all cases with a cell size of 5 µm and 3 µm, respectively in the y and z

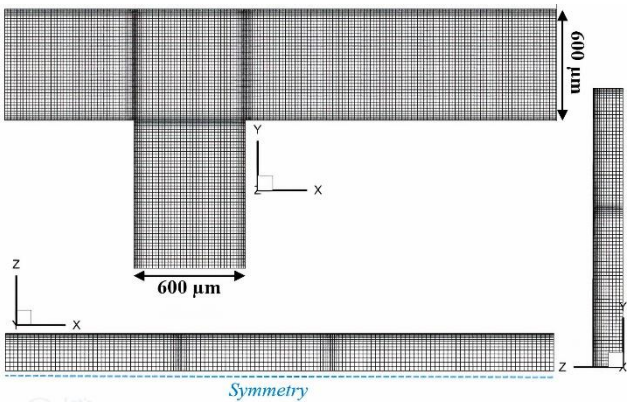

Fig. 3 Meshing of the microchannel (T-junction)

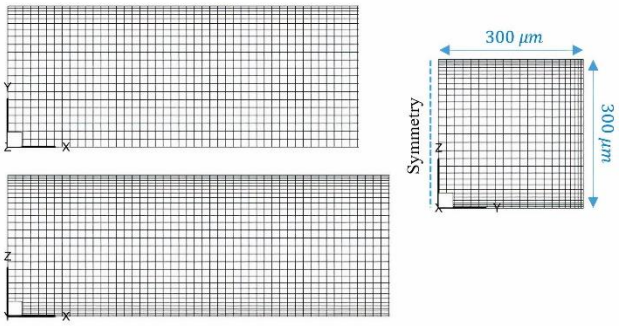

Fig. 4 Meshing of the microchannel (Patching method)

directions. In addition, we maintained an aspect ratio of 1 far from the channel walls (cubic mesh elements). Gupta et al. (Gupta et al., 2009) stated that cubic mesh elements for 3D simulations minimise uncertainties and prevent spurious currents from being generated (Fig. 3 and 4).

An inlet velocity of U_{TP}=0.037 m/s was chosen to study the mesh independence. Using ethylene glycol as a continuous phase, the water patch with a length of 1.1 mm was placed about 1 mm from the channel inlet.

For the different meshes, we compared the results of the normalized longitudinal velocity in the *y* and *z* directions (Fig. 5 and 6) and pressure drop along the plug (Fig. 7).

Figures 5 and 6 show that the four mesh sizes give almost the same results near the wall. However, when moving towards the microchannel centre (along the y-axis or the z-axis), the 17 µm, 12 µm, and 7 µ*m* mesh sizes give better results in terms of longitudinal velocity than the 25 µm mesh size. On the other hand, as shown in Fig. 7, there is no significant variation among the four mesh sizes regarding pressure drop. However, the two meshes (7, 12, and 17 µm) provide slightly more accurate results.

To save computational cost while ensuring better results quality, the 17 um mesh size was chosen for the remaining analysis. The same mesh size will be used for the T-junction approach, using the same mesh refinement along the y- and z-axes (5 µm along the y-axis and 3 µm along the z-axis) as discussed above.

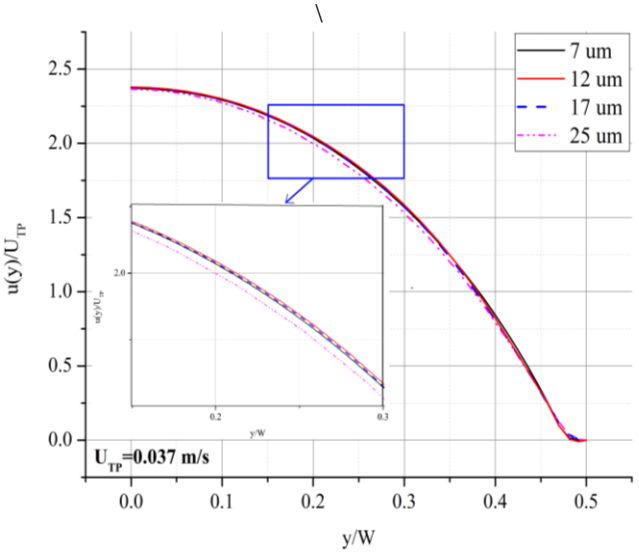

Fig. 5 Longitudinal velocity profile along the y-axis for different mesh sizes

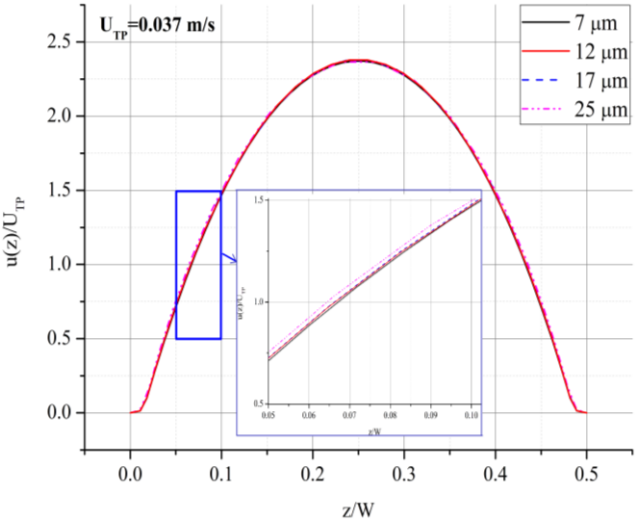

Fig. 6 Longitudinal velocity along the z-axis for different mesh sizes

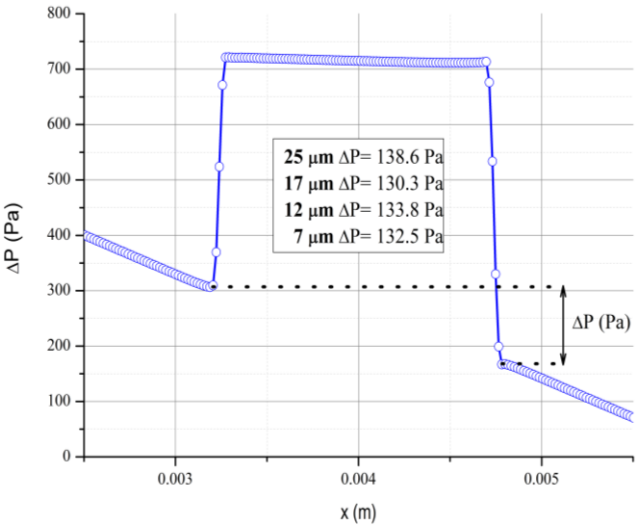

Fig. 7 Pressure drop for different mesh sizes

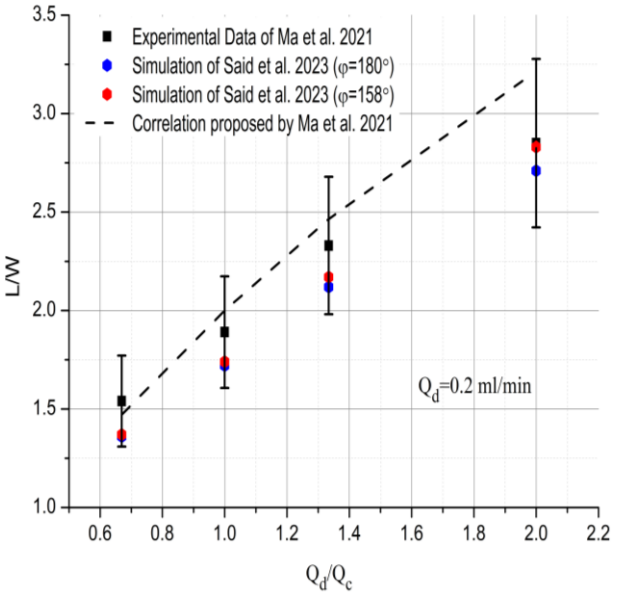

Fig. 8 Validation of the T-junction method using the experimental results of Ma et al (Ma et al., 2021) and their correlation

3. RESULTS AND DISCUSSION

3.1 Validation

All in this section, we validate the Patching method by comparing its obtained results with those of the T-junction method. The comparison is performed in terms of the liquid film thickness (in the corners δ_{Cr} and the near wall region δ_y), the curvature radius of the front and back of the plug "R_{front}; R_{tail}" (shape of the plug).

For the T-junction method, the model was successfully validated in our previous work (Said et al., 2023). The validation was done by comparing the droplet/plug length obtained by our simulations with Ma et al.'s correlation and experimental results (Ma et al., 2021) (See Fig. 8).

The comparison results were performed for a flow rate ratio q range from 0.5 to 2. Note that the dispersed phase flow rate was kept constant (Q_d=0.2 ml/min), and only the continuous phase flow rate (Q_c) was varied. In the case of partial wetting of the working fluids with the microchannel walls (the same as in the study by Ma et al.), the relative error for each flow rate ratio did not exceed 15%, with an average relative error of 7%.

We selected two fluid combinations for the comparative study. We chose firstly the combination of ethylene glycol and water (**EG/W**). To further extend our comparative study, a second fluid combination, namely propylene glycol and water (**PG/W**) was employed. Table 2 shows the input parameters used for the two methods.

Where L_0, l_0, U_{TP}, U_c, U_d, q are, respectively, the water patch length, the distance between patches, the mixture velocity, the continuous phase velocity, the dispersed phase velocity, and the flow rate ratio (See Fig. 9).

It is worth mentioning that the input parameters (patch length L_0, distance between patches l_0) for the patching method must be adjusted to provide the same plug/plug length as for a T-junction method. The tables below (Tables 3 and 4) show the results of this comparative study.

According to Table 3, the results obtained by the patching method, whether in terms of liquid film, plug shape or plug/slug length, agree well with the results obtained by the T-junction method.

Table 4 shows the liquid film thickness results obtained by the T-junction and the patching methods. Note that these results were determined at the mid-axis droplet where the liquid film is constant.

For the liquid film in the corners (δ_{Cr}), the patching method gives satisfactory results for both liquid combinations, with a relative error of no more than 2%.

However, for the liquid film at the sidewalls (δ_z), the relative error was around 15% for both liquid combinations. Note that δ_z was difficult to obtain because of the small thickness of the liquid film in this section.

To further illustrate the reliability of the patching method, we performed a comparison based on the liquid film obtained by the patching method, both in the corners (δ_{Cr}) and close to the top wall (δ_y), against the experimental correlations presented in Table 5 and the numerical results of Said et al. (2023) (See Fig. 10).

Table 2 The input parameters for both methods

	Patching method			T-junction method		
Fluid combination	L_0 (mm)	l_0 (mm)	U_{TP} (m/s)	U_c (m/s)	U_d (m/s)	q
EG/W	1.1	1.445	0.037	0.0185	0.0185	1
PG/W	0.84	1.36	0.037	0.0185	0.0185	1

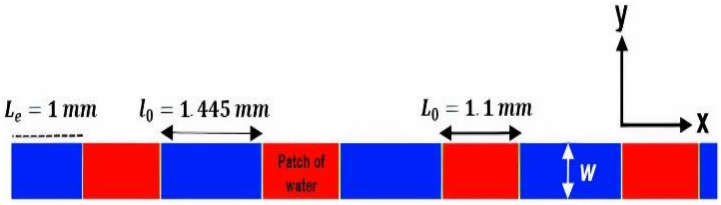

Fig. 9 Input parameters for the patching method for EG/W

Table 3 A comparison between the T-junction and patching methods for the two chosen combinations

Fluid combination	*Method*	*Studied parameters*			
		Droplet/slug length		Droplet shape	
		L_D/W	L_s/W	R_{tail}/W	R_{front}/W
EG/W	T-junction	2.35	1.76	$5.06 \cdot 10^{-1}$	$4.05 \cdot 10^{-1}$
	Patching	2.43	1.68	$5.09 \cdot 10^{-1}$	$4.13 \cdot 10^{-1}$
	Deviation %	**3.4**	**4.5**	**1.9**	**0.6**
PG/W	T-junction	2.08	1.53	$4.8 \cdot 10^{-1}$	$3.63 \cdot 10^{-1}$
	Patching	2.07	1.48	$4.79 \cdot 10^{-1}$	$3.7 \cdot 10^{-1}$
	Deviation %	**0.5**	**3.2**	**1.9**	**0.2**

Table 4 Liquid film results (δ_y, δ_z, δ_{Cr}) for both methods

Fluid combination	*Method*	*Studied parameters*		
		δ_y/W	δ_z/W	δ_{Cr}/W
EG/W	T-junction	0.015	0.006	0.1109
	Patching	0.014	0.0067	0.1112
	Deviation %	**6**	**14**	**0.3**
PG/W	T-junction	0.0433	0.01	0.134
	Patching	0.0408	0.017	0.136
	Deviation %	**5.7**	**15**	**1.5**

Table 5 Experimental correlations of liquid film thickness

Correlation	Operation condition	Reference
$\frac{\delta_y}{W} = 0.15[1 - exp(-8.221Ca_D^{0.972})]$	Rectangular microchannel $0.00065 < Ca_D < 0.3$	Yao et al. (2019)
$\frac{\delta_{Cr}}{W} = 0.249 - 0.182\exp\left(-13.9Ca_D^{0.944}Re_{TP}^{-0.202}\right)$	Rectangular microchannel $0.0003 < Ca_D < 0.15$	Ma et al. (2021)
$\frac{\delta_{Cr}}{W} = 0.35 - 0.25\exp\left(-2.25Ca_D^{0.445}\right)$	Square channel $Ca_D < 3.0$	Kreutzer et al. (2005)

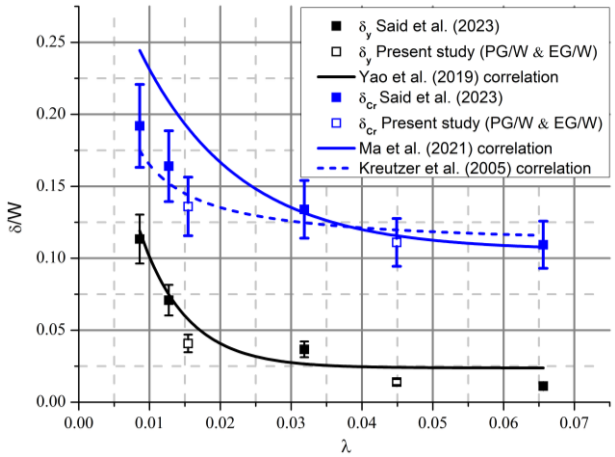

Fig. 10 Summary of results obtained on the evolution of δ_y and δ_{Cr} versus the viscosity ratio

To do this, we chose for δ_y the correlation of Yao et al. (2019), originally performed for gas-liquid systems in a rectangular microchannel (the same geometry as our). Whereas for δ_{Cr}, we selected two correlations, one developed by Ma et al. (2021) and the other by Kreutzer et al. (Kreutzer et al., 2005). The Ma et al. (2021) correlation was designed for liquid-liquid systems in rectangular microchannels (the same channel size as our), while the Kreutzer et al. (2005) correlation was first developed for gas-liquid systems in square microchannels.

Figure 10 provides a comparative analysis of the liquid film results obtained by the patching method with the experimental correlations available in the literature (Table 5) and the numerical results of Said et al. (Said et al., 2023). We can see that the liquid film thickness results (δ_{Cr}, δ_y) obtained by the patching method reasonably agree with the numerical data of Said et al. (2023).

Regarding the liquid film in the corners, the results obtained by the patching method and the numerical results of Said et al. are in excellent agreement with the experimental correlation of Kreutzer et al. (Kreutzer et al., 2005), regardless of the viscosity ratio λ. The average relative error between the numerical results of δ_{Cr} and the experimental correlation of Kreutzer et al. (Kreutzer et al., 2005) does not exceed 4.5%. Compared with the experimental correlation of Ma et al. (2021), the numerical results of δ_{Cr}, whether those obtained by the patching method (hollow square) or the numerical results of Said et al.(2023), agree well at high viscosity ratios λ. However, as λ increases, the numerical results of δ_{Cr} deviate from the correlation of Ma et al. (2021), with an average relative error of 14%.

For the liquid film δ_y, the numerical results show a good agreement with the correlation of Yao et al. (2019) at low viscosity ratio λ. The average relative error between the numerical results of δ_y and the experimental correlation of Yao et al. (2019) is 17%.

Table 6 Dimensionless liquid film thickness (δ_y/W) by patching method versus experimental correlations

Fluid combination	δ_y/W		
	Patching method	Yao et al. (2019) correlation	Deviation %
EG/W	0.014	0.022	36
PG/W	0.0408	0.0426	4

In the following, we will focus our analysis on the liquid film obtained by the patching method.

For the EG/W combination, the liquid film thickness along the y-axis δ_y (Table 4 or Table 6) is 1.4%W the channel width, while for the PG/W combination, the liquid film along the y-direction is 4.08%W. Therefore, the fluid flow rate passing through the liquid film region is higher in the case of PG/W compared to EG/W. However, this could be a disadvantage for heat and mass transfer because increasing the liquid film thickness δ causes a decrease in the intensity and volume of the recirculation zone. The same conclusions were reported earlier by Abadie et al. for a gas-liquid system (Abadie et al., 2013).

Along the z-direction (See Table 4), the liquid film in the EG/W case was 1.33% of the microchannel height, compared to 2.3%h in the PG/W case. Thus the plug is more confined (along the z-axis) in the EG/W case than in the PG/W case.

Table 6 presents the liquid film δ_y resulting from the patching method with the experimental correlation of Yao et al. (2019). From Table 6, we can see that the liquid film in the near wall region (δ_y) is overestimated by the correlation of Yao et al. (2019) for the EG/W combination. Abdollahi et al. (2020) and Ma et al. (2021) noticed the same result and stated that for $Ca_D < 0.03$ (based on plug velocity U_D), the liquid film is smaller compared to the correlation predictions. The viscous stress exerted by the dispersed phase on the film interface could be a possible reason, especially when we know that the dispersed phase in liquid-liquid systems is generally more viscous than gases. It is worth mentioning that the capillary number (Ca_D) for the EG/W combination is 0.0173, while for PG/W, the Ca_D is 0.037.

To date, there is no single correlation in the literature capable of predicting the wall liquid film thickness (δ_y) for liquid-liquid systems with fluid combinations having low viscosity ratios in rectangular microchannels. Further studies are required in this field.

Table 7 Dimensionless liquid film by patching method versus experimental correlations

Fluid	δ_{Cr}/W				
	Patching	Ma et al. (2021)	**Deviation %**	Kreutzer et al. (2005)	**Deviation %**
EG/W	0.111	0.116	4	0.118	6
PG/W	0.136	0.168	19	0.134	2

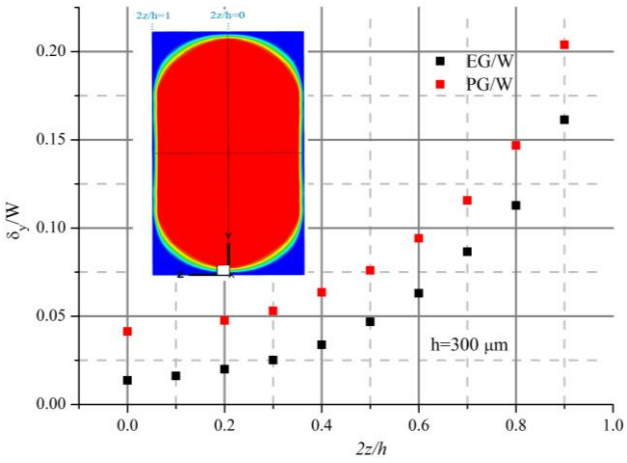

Fig. 11 Variation of the dimensionless liquid film thickness (δy/W) along the z-axis for both fluid combinations

Regarding the liquid film thickness at the corners δ_{Cr} (Table 7), we observed a good agreement with the correlations for both EG/W and PG/W combinations. The relative error, for the EG/W combination, compared to the correlations of Ma et al. (2021) and Kreutzer et al. (2005) was 4% and 6%, respectively while for the PG/W combination, the relative error was 19% when compared to Ma et al.'s correlation (Ma et al., 2021) and 2% for Kreutzer et al.'s correlation (Kreutzer et al., 2005).

Figure 11 illustrates the variation of liquid film thickness δ_y along the z-axis for the EG/W and PG/W cases. At first glance, it is evident that the liquid film thickness δ_y for PG/W case is thicker than that of the EG/W case.

For *2z/h=0* (the middle of the cross-section), the liquid film thickness δ_y is minimal for both fluid combinations. However, once approaching the sidewalls, δ_y gradually increases, increasing the leakage flow of the continuous phase (corner region).

On the other hand, Fig. 12 represents the variation of the dimensionless liquid film thickness (δ_Z/W) along the y-axis for both fluid combinations (EG/W and PG/W).

As can be seen, the dimensionless liquid film thickness (δ_Z/W) at 2y/W=0 is small regardless of the fluid combination, with δz/W of the EG/W combination slightly higher than that of PG/W by a few micrometers.

Even if $2y/W$ increases progressively ($0 < 2y/W \leq 0.5$), the dimensionless liquid film (δ_Z/W) remains constant for both cases, indicating an effective confinement of the water plug along the y-axis. Starting at 2y/W>0.5, the liquid film δ_z progressively increases until it reaches a maximum around 2y/W=0.9 for both fluid combinations. This region of liquid film variation is known as gutters (microchannel corners).

3.2 Droplet Shape

One of the advantages of microfluidics is the ability to control the volume and shape of the droplet through the control of parameters such as the flow rate ratio (q) and mixture velocity (U_{TP}). In this section, we compare the

Table 8 Dimensionless front and rear curvature radii of the plug for both methods

Fluid combination	Plug shape	T-junction	Patching	Deviation %
EG/W	R_{front}/W	$4.05 \cdot 10^{-1}$	$4.13 \cdot 10^{-1}$	2
	R_{tail}/W	$5.06 \cdot 10^{-1}$	$5.09 \cdot 10^{-1}$	1
PG/W	R_{front}/W	$3.63 \cdot 10^{-1}$	$3.70 \cdot 10^{-1}$	2
	R_{tail}/W	$4.8 \cdot 10^{-1}$	$4.79 \cdot 10^{-1}$	1

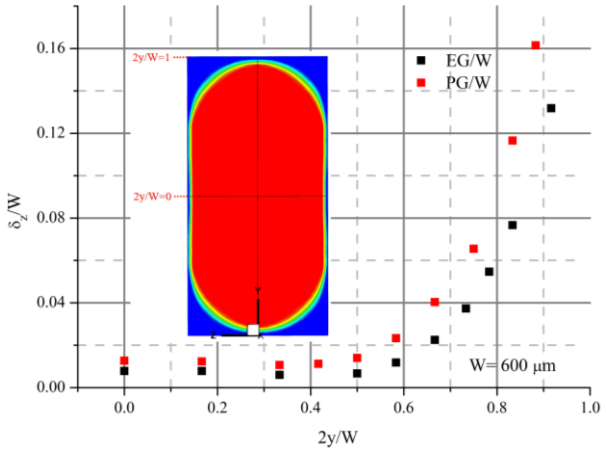

Fig. 12 Variation of dimensionless liquid film thickness (δz/W) along the y-axis for both fluid combinations

plug shape through the curvature radii of the front and back of the plug (R_{tail}; R_{front}) for both methods (*T-junction* and *patching*) (See Table 8).

As can be seen in Table 8, the dimensionless curvature radii R_{tail} and R_{front} obtained by the patching method show almost similar results to those obtained by the T-junction method, with a relative error of no more than 2%.

Thus, both methods show almost the same water plug shape, regardless of the fluid combination (EG/W and PG/W).

Figure 13 presents the plug shape in the XY plane for both the T-junction and the patching methods.

As shown in Fig. 13, there is no difference in plug shape between the T-junction method and the patching method for both fluid combinations, indicating the reliability of the patching method. In addition, the water plug is more confined along the y-axis for the EG/W combination than for the PG/W combination.

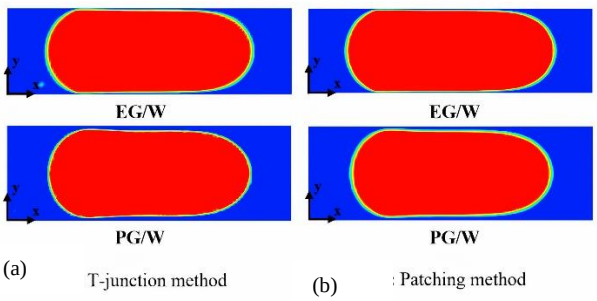

Fig. 13 Water plug shape in XY plan for both numerical methods

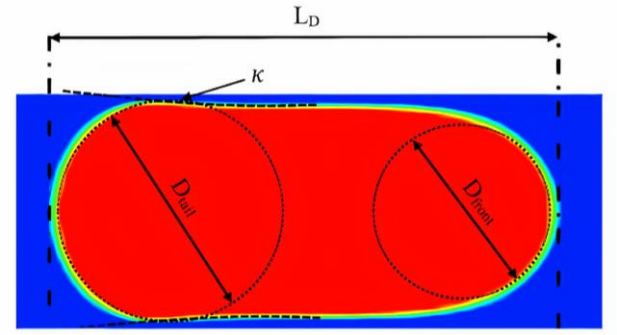

Fig. 14 Illustration of plug shape for the PG/W combination (Patching method)

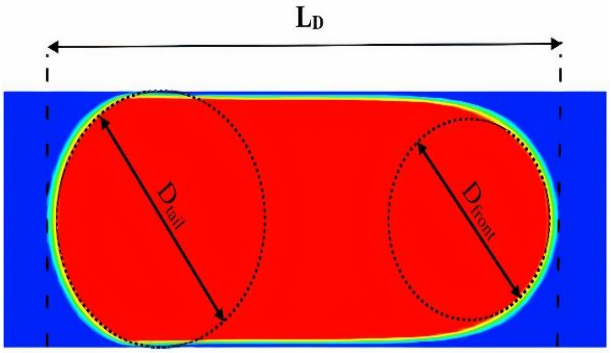

Fig. 15 Illustration of plug shape for EG/W combination (Patching method)

For the PG/W flow case, we noticed a concave surface on the lateral side of the plug interface (See Fig. 14), which was not the case for the EG/W combination (See Fig. 15).

Wang et al. (2021) reported the same observation in their study and attributed it to the dominance of interfacial tension on the plug interface over viscous and inertial forces (low capillary number). They believe that the dominance of interfacial tension causes the shrinkage of the plug interface on the lateral side near the plug tail.

3.3 Droplet Formation Mechanism

3.3.1 T-Junction Method

The T-junction is one of the most widely used microfluidic devices for drop/plug generation. Indeed, Dessimoz et al. (2008) were among the first to use it to study flow patterns.

The T-junction consists of a main and secondary channel intersecting at a 90° angle. The fluid that wets the channel walls is called the continuous phase (ethylene/propylene glycol in our case) and enters through

the main channel. On the other hand, the phase that presents poor wettability is called the dispersed phase (water) and enters through the secondary channel. Once droplets are formed, a liquid film appears in the near-wall region. This film separates the dispersed phase from the microchannel walls.

Flow patterns result from the competition between the different forces (interfacial, viscous, inertial) at the junction. This competition between forces is characterized by dimensionless numbers such as Capillary *Ca*, Reynolds *Re* and Weber *We*. Note that the gravitational forces are negligible, because the Bond number ($Bo = \Delta\rho g D_h^2/\sigma$), expressing the ratio between the gravitational and interfacial forces, is too small.

The droplet/plug flow pattern appears when the surface tension force predominates over viscous and inertial forces. Four main droplet/plug formation mechanisms could be distinguished (squeezing, transition, dripping, and jetting). In the squeezing regime (low Ca), the dispersed phase tip penetrates and completely blocks the main channel. In addition, the plugs formed have a diameter longer than the microchannel width. According to the literature, plug size in the squeezing regime doesn't depend on the fluid properties (e.g. working fluid viscosities, interfacial tension...) and only the flow rate ratio controls the plug size (Garstecki et al., 2006; De menech et al., 2008). However, in the dripping regime, the dispersed phase head partially blocks the main channel. Thus, the continuous phase flows faster through the gap between the dispersed phase head and the top wall. As a result, high viscous shear is applied to the emerging droplet, thus accelerating the droplet formation process, resulting in droplets with a diameter smaller than the channel width.

We selected the fluid combination (EG/W) to examine the droplet/plug formation mechanism. The flow rate of the continuous and dispersed phases is the same (Q_d=Q_c=*0.2 ml/min*), giving a flow ratio of *q=1*.

Table 9 presents the dimensionless parameters for both the continuous and dispersed phase. Given the continuous phase *Ca* number, plug formation in our study occurs in the transient regime (between the squeezing and dripping regimes).

In this regime, the plug formation process is always governed by the pressure build-up upstream of the junction *"Squeezing process"*, but this time with the help of viscous shear exerted by the continuous phase on the emerging plug through the gutters as well as the gap between the dispersed phase head and the upper wall (see Fig. 16c).

Table 9 Dimensionless parameters for the two phases

Phase	$Ca_i = \mu_i U_i/\sigma$	$Re_i = \rho_i U_i D_h/\mu_i$	$We_i = \rho_i U_i^2 D_h/\sigma$
Continuous phase	$7.64 \cdot 10^{-3}$	0.41	/
Dispersed phase	/	8.3	$2.85 \cdot 10^{-3}$

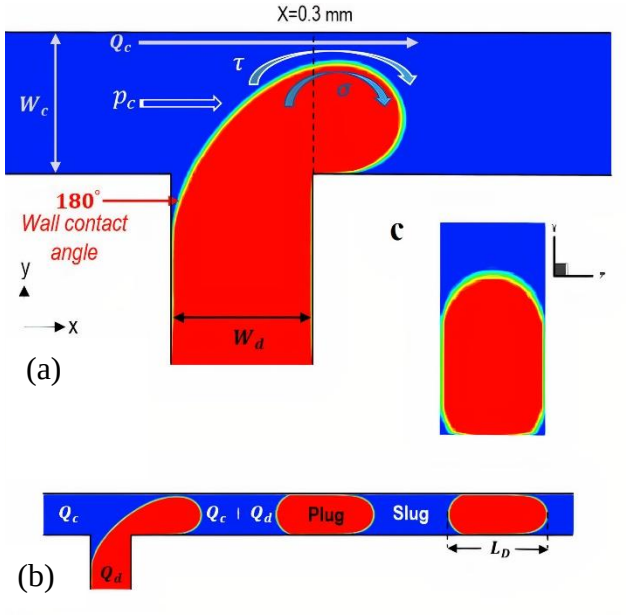

Fig. 16 Droplet formation process: (a) squeezing phase, (b) droplet formation mechanism and droplet development

To fully understand this, we perform a simple analysis using the dimensionless numbers shown in Table 9. Looking at the Reynolds numbers of the two phases, we can see that viscous forces dominate the continuous phase flow *"Ethylene glycol"*, while inertial forces dominate the dispersed phase flow "*water*". However, to understand the dominant force in the droplet formation process, we compare these two forces (viscous and inertial) with the interfacial tension forces. So, we calculated the capillary number of the continuous phase, which is the ratio between the viscous forces and the interfacial tension forces, and the Weber number of the dispersed phase, which is the ratio between the inertial forces and the interfacial tension forces.

We can see from Table 9 that interfacial tension dominates both the viscous forces of the continuous phase and the inertial forces of the dispersed phase. Based on that, we can conclude that the interfacial tension force is the dominant force in the droplet formation process and that the pressure built up upstream of the junction is the main reason for droplet detachment, with the help of the viscous shear of the continuous phase.

Two essential steps, filling and squeezing are observed in the plug formation mechanism in the transitional regime. In the filling stage, the tip of the dispersed phase penetrates into the main channel and partially blocks it. Simultaneously, pressure rises upstream of the junction (Fig. 18 and 19).

Figure 17 presents a cross-section of the remaining gap between the emerging droplet and the main channel top wall at the end of the filling stage and just before the squeezing stage for the EG/W combination. The cross-section was chosen close to the junction at the location of droplet detachment.

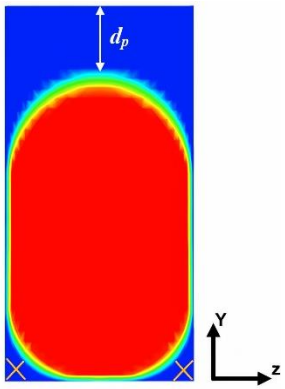

Fig. 17 A cross-section presenting the gutters and the gap between the emerging droplet and the top wall at the junction

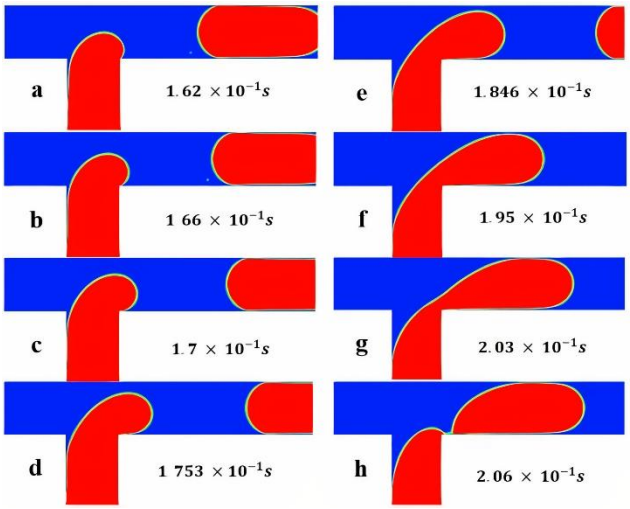

Fig. 18 Droplet formation mechanism under the transition regime

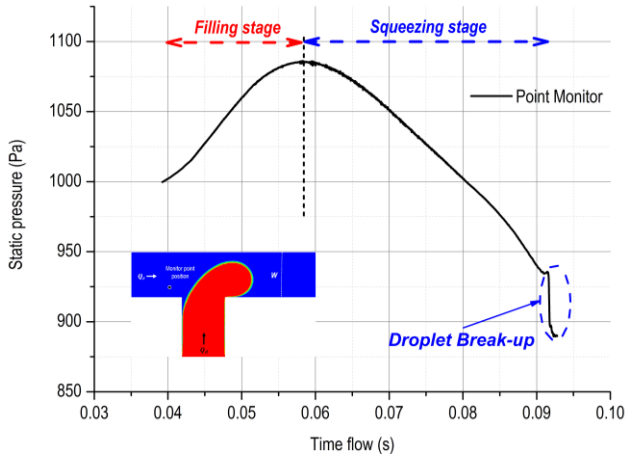

Fig. 19 Static pressure variation upstream of the junction during droplet formation processes

According to Li et al. (2012), the gutters near the bottom wall (see Fig. 17) could also contribute to the droplet formation process through the shear exerted by the continuous phase as it passes through. Van Steijn et al. (2007) reported in their study that for a channel with an aspect ratio equal to unity, 25% of the continuous phase flow rate (a leakage flow) passes through the gutters as well as the gap between the microchannel top wall and the emerging droplet. For the EG/W combination and a continuous phase Ca number of 0.00764 (low Ca), the emerging droplet approaches the microchannel sidewalls with only a thin continuous liquid film separating the emerging droplet from the sidewalls. The same observations were reported by Li et al. (2012) for low Ca number (less than 0.01), with a smaller gap between the top wall and the emerging droplet than that found in our simulations.

During the second stage (squeezing stage), the pressure built up upstream of the junction accompanied by viscous shear causes the squeezing of the neck connecting the plug to the dispersed phase. As a result, the plug separates from the dispersed phase (Li et al., 2012; Yan et al., 2012).

This formation process is simultaneously and periodically repeated. We define T_f as the droplet formation period, introduced as the time required for a unit cell (*plug and slug*) to pass through a given cross-section. L_D, L_s, and U_D are respectively the plug length, the slug length, and the droplet velocity.

$$T_f = (L_D + L_s)/U_D \tag{10}$$

In our case, the plug formation period T_f is 0.057 s and agrees well with that obtained from expression 10 giving a value of 0.058 s. This reflects the reliability of the numerical model.

In Fig. 20, we represent the duration of the filling stage ($t_{filling}$) and the squeezing stage ($t_{squeezing}$) as a function of the neck diameter dimensionalised by the microchannel width (D_{neck}/W).

It's worth mentioning here that D_{neck} is measured at the location of the channel where the breakup occurs (see Fig. 21). Fig 20 clearly shows that the squeezing time is significantly greater than the filling time. Furthermore, the transition from the filling to the squeezing stage occurs once the neck diameter reaches its maximum. For $0.1 < \lambda < 10$, Nekouei and Vanapalli (2017) demonstrated that $t_{Filling}$ is independent of Ca and viscosity ratio λ, contrary to $t_{squeezing}$. To our knowledge, none of the previous studies have examined the filling and squeezing stage for $\lambda < 0.1$.

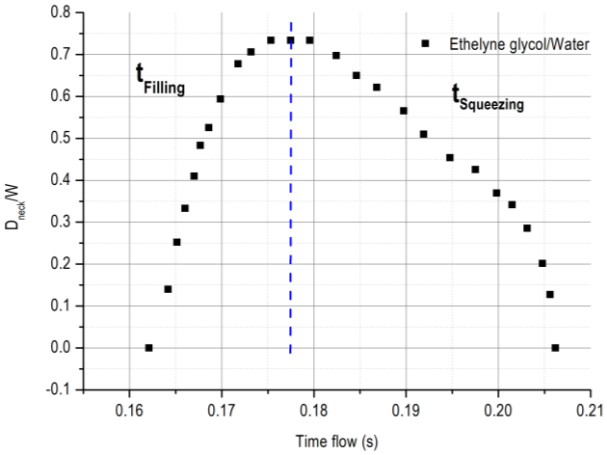

Fig. 20 Evolution of D_{neck} versus flow time

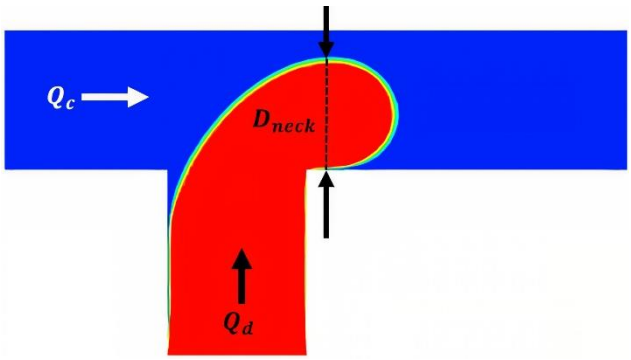

Fig. 21 Location of D_{neck} measurement

Figure 22 shows the filling and squeezing stage for three different parameters. These are the flow rate ratio q, the viscosity ratio λ, and the capillary number based on the mixture velocity U_{TP} (Ca_{TP}). For each studied parameter, remainders are kept constant.

The filling and squeezing stage were obtained by instantaneously measuring the volume fraction of the dispersed phase at the location where the breakup occurred.

As shown in Fig. 22, the filling stage is independent of the viscosity ratio λ and Ca_{TP} number. This is in agreement with Nekoui et al's previous observations (Nekouei & Vanapalli, 2017). However, for different flow rate ratios q, a slight difference was observed in the filling stage when changing from a flow rate ratio of 0.5 to 1.

For various Ca numbers (Ca_{TP}), the squeezing time is almost the same, with a slightly longer squeezing time for Ca_{TP}=0.03305. Nevertheless, for t/t_{max} =0.2, the neck diameter of the dispersed phase (in terms of volume fraction) for Ca_{TP}=0.0330 is smaller than for Ca_{TP}=0.0165. One explanation for this is that increasing the velocity of both phases while keeping the same flow rate ratio causes both an increase in the viscous and inertia shear of the continuous phase. To check this, we calculated the continuous phase Ca_c number (based on continuous phase velocity U_c) for both Ca_{TPs} and found that the Ca_c for Ca_{TP}=0.0330 (Ca_c=0.0165) was as high as that for Ca_{TP}=0.0165 (Ca_c=0.00826).

When varying the viscosity ratio λ or the flow rate ratio q, the squeezing process (or the way the neck diameter is compressed) follows the same pattern. However, the squeezing time is greatly affected by the change in the flow rate ratio q compared with the viscosity ratio λ. One reason for this is that at q=1, the continuous and dispersed phase velocities are the same, while at q=0.5, the continuous phase velocity is two times greater than that of the dispersed phase. This superiority in the continuous phase velocity U_c causes an increase in the viscous forces (expressed by the Ca_c number), leading to a faster squeezing stage and, therefore, to water plug detachment. However, when the viscosity ratio is changed, the continuous phase Ca number does not change significantly (Cac=0.00826 for λ=0.04488 and Cac=0.00824 for λ=0.01546), which explains the small effect of the viscosity ratio on the squeezing time (see Fig. 22).

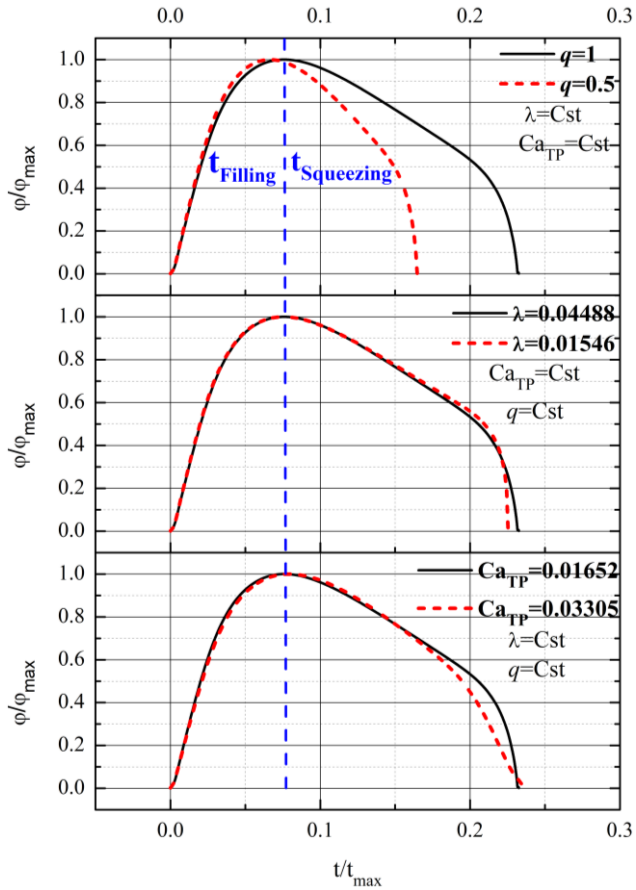

Fig. 22 Filling time and squeezing time versus Q, Ca_{TP}, and λ

3.3.2 Patching Method

The patching method also falls into the category of methods using a stationary frame of reference (laboratory frame). Consequently, it requires more computational time than those using a moving frame of reference (a referential moving with the droplet). In the present work, we implemented a straight, horizontal 3D microchannel with a cross-section (the same as the T-junction) of 600 μm × 300 μm.

A constant flow rate of ethylene glycol is applied at the inlet, corresponding to a velocity of U_{TP}=0.037 m/s ($U_{TP}=U_c+U_d$).

It is worth mentioning that the patching method does not involve any of the most common geometries (e.g. T-junctions and Y-junctions) for droplet/plug formation. Although the patching method is computationally less time-consuming than the T-junction method, it does not allow the observation of the droplet/plug formation process, which removes a large part of Taylor's flow hydrodynamics in the microchannels.

To create water drops, we mark a zone close to the channel entrance immediately after a distance (L_e) dedicated to the inlet flow development. Four quadrilateral zones were marked as initial water droplets. Each zone has an initial length of 1.1 mm (initial droplet length) with a width and height equal to those of the microchannel (W=0.6 mm; h=0.3 mm). Additionally, the distance between patches was 1.445 mm. These parameters were

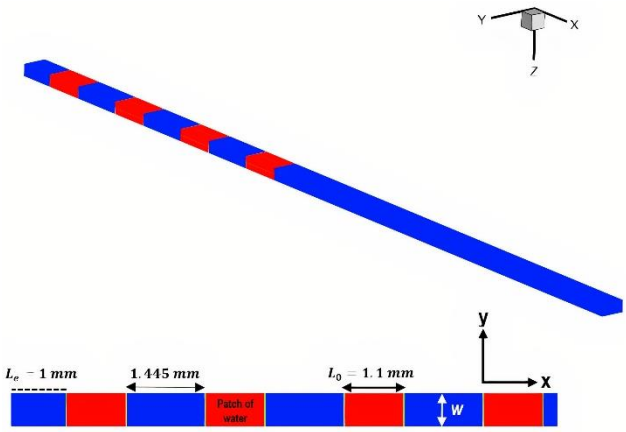

Fig. 23 Initial conditions for the patching technique

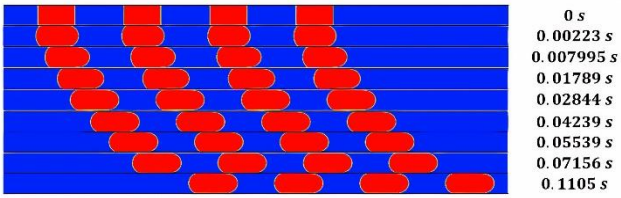

Fig. 24 Development and preparation stage of the water patches

chosen to obtain the same droplet and slug length generated by the T-junction method (see Fig. 23).

The initialized water droplets require some time (t_{dev}) to become fully developed droplets (see Fig. 24). As we progress through the channel (*t=0.00223 s*), the front and tail of the plug start to have a certain degree of curvature with slight larger curvature radii at the plug tail than at the front one. According to the literature (Eain et al., 2013), the plug's shape is maintained through the balance between the pressure within the plug and the interfacial tension.

With further progression in the channel (*t=0.01094 s*), a liquid film of ethylene glycol gradually appears and extends towards the droplet tail, eventually separating the droplets from the channel walls by two thin liquid films (see Fig. 25).

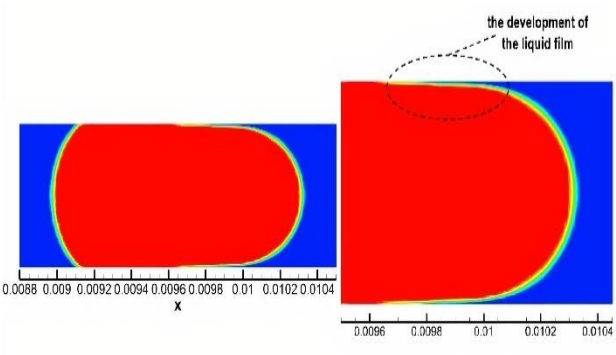

Fig. 25 Development of the liquid film in the near wall region

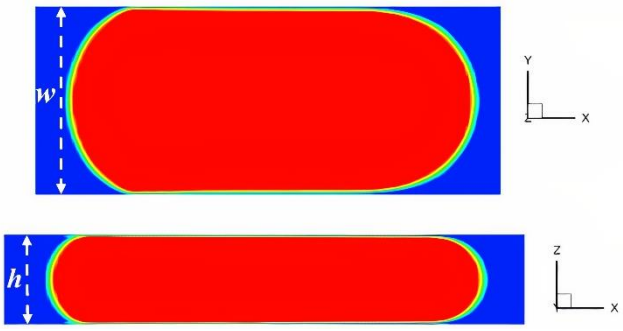

Fig. 26 Final droplet shape in the *xy* and *xz* plane

Table 10 L_D, R_{front}, R_{tail} dimentionalised by the channel width W, for different flow time

EG/W combination					
t=0.0800722 s			*t=0.104125 s*		
L_D/ W	R_{front}/ W	R_{tail}/ W	L_D/ W	R_{front}/ W	R_{tail}/ W
2.42	0.515	0.401	2.43	0.508	0.402

The following stage concerns the stabilisation of the liquid film and the droplet's front and tail, as can be seen in Fig. 26. To follow full droplet development, we calculate droplet length and their curvature radius at the front and rear for different flow times (t=0.104125 s and t=0.0800722 s).

After the first step “development step”, four key parameters could be determined, namely the development step duration t_{dev}, the droplet/plug and slug length (L_D, L_s), the liquid film thickness (δ_y,δ_z,δ_{Cr}), and the curvature radii of the droplet/plug front and back (R_{front}, R_{tail}).

The results were almost identical, indicating that droplets had attained their final shape (See Table 10).

Our observations regarding the droplet length indicate that L_D after development is slightly longer than the initial droplet length L_0. This is mainly due to droplet development in the corners and the liquid film region. Once the droplets reach the channel outlet, the simulation can be considered complete and manually stopped.

3.4 Flow Field Inside Water Plug and Near the Interface

Slug flow (also known as Taylor flow) is one of the most stable flows, allowing for better heat and mass transfer performance. Our purpose in this section is to explore the flow field in a unit cell composed of a water plug in the center and two half-slugs on either side.

Figure 27 represents the contours of the x-velocity component *u(y)* and the streamlines within the water plug and in the vicinity of the interface separating the two liquids for various 2z/h. Note that 2z/h=0 refers to the middle of the cross-section "*plug centre*", where the liquid film thickness along y and z is minimal (δ_y, δ_z). In contrast, 2z/h=0.8 is located near the sidewall (see Fig. 11).

At the 2z/h=0 section, we can see the presence of a backflow in the liquid film region, characterized by

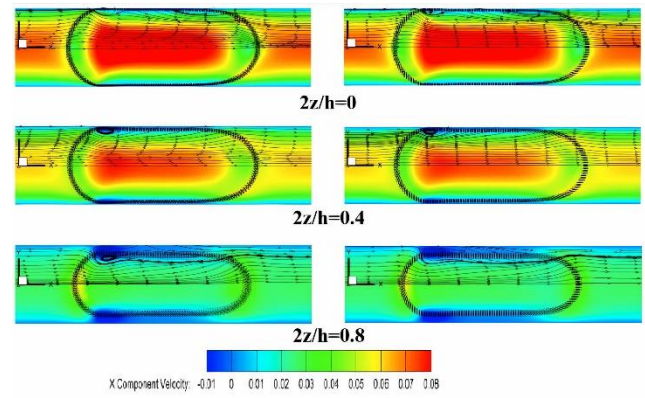

Fig. 27 Contours of the x-velocity component u(y) for various sections along the z-axis and for both the T-junction and patching methods (EG/W case)

negative longitudinal velocity (The blue region). As we move towards the center of the microchannel, the x-velocity component becomes positive and gradually increases, reaching a maximum at y/W= 0, whether inside the water plug or in the slug region. These negative velocity areas can also be detected in the streamline contours, where a vortex appears at the interface near the water plug's tail. The formation of vortices in water slugs reveals that the shear stress in the wall vicinity is reversed relative to the bulk flow.

Moving towards the side wall, along the z-axis (2z/h=0.4), the intensity of *u(y)* decreases, with a maximum velocity remaining at the microchannel centre. Furthermore, an increase of the backflow zone in the liquid film region is observed, mainly due to the increase in the liquid film thickness (see Fig. 11). This backflow zone rises further as the liquid film thickness continues to increase (2z/h=0.8), causing an increase in the vortex size occurring near the water plug tail. Besides, we also noted a decrease in the x-velocity intensity, meaning that the microchannel sidewall was getting closer and closer (2z/h=0.8).

Figure 28 illustrates the positions chosen for velocity profiles before and after the water plug. Sections 1 and 5 were positioned 0.88W away from the interface of the two fluids, whereas sections 2 and 4 were 0.42W away from the plug interface.

Figure 29 shows the velocity profiles for the EG/W combination at different positions in a unit cell (a plug and half a slug on each side) for the two methods (T-junction and patching). The velocity profiles were plotted in the same sections (2z/h=0, 2z/h=0.4, and 2z/h=0.8) presented in Fig. 27.

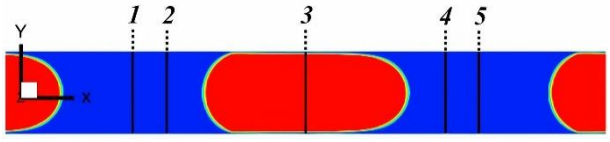

Fig. 28 Selected sections for collecting the *u(y)* velocity profiles

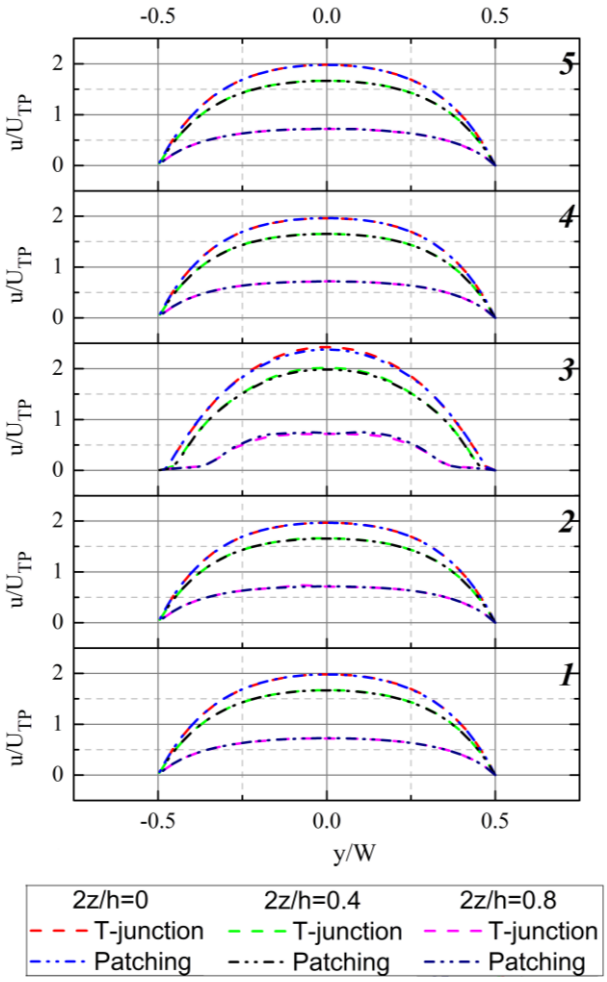

Fig. 29 Velocity profiles *u(y)* at various positions before and after the water plug for both methods (EG/W case)

It is clear from Fig. 29 that the velocity profiles at 0.88W and 0.42W from the water plug or in the water plug centre are similar no matter the method used, i.e., the profiles overlap.

Figure 29 also confirms the observations made in Fig. 27. As we move from 2z/h=0 to 2z/h=0.8 (along the z-axis), the x-velocity component decreases progressively regardless of the section selected.

For 2z/h=0.8 and in section 3 (at the water plug centre), we can notice the presence of a low *u*-velocity region in the velocity profile at the side walls compared to the other two sections (2z/h=0 and 2z/h=0.4). This low *u*-velocity zone corresponds to the liquid film region.

We can also see that the velocity profiles in the half slugs (before and after the plug) are flattened compared with the velocity profile in the center of the water plug, with a maximum always located at the microchannel centre. As you approach the top or bottom walls of the microchannel, the velocity gradually decreases until it reaches its lowest value.

Figure 30 illustrates the velocity magnitude contours with the streamlines along the XZ plane for both T-junction and the patching methods. We choose three sections along the y-axis. The first section (2y/W=0)

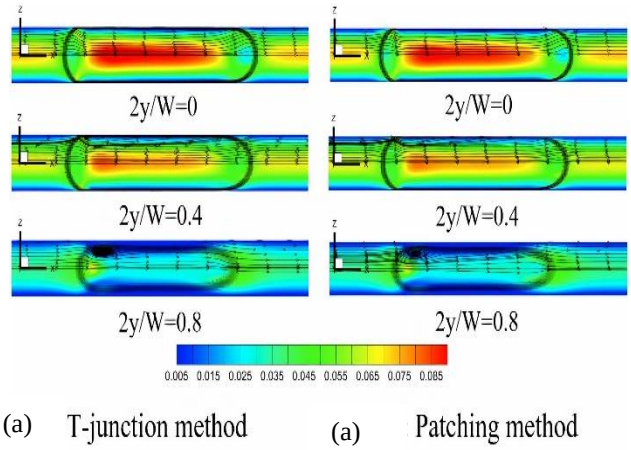

Fig. 30 Contours of the magnitude velocity for various sections along the y-axis and for both the T-junction and patching methods (EG/W case)

corresponds to the microchannel centre (see Fig. 12), while the 2y/W=0.8 section is close to the top wall.

As can be seen, 2y/W=0, the velocity magnitude is highest at the microchannel centre inside the water plug, for. We can also notice an area of low velocity magnitude in the plug's head and tail. In the half-slug before and after the water plug, the velocity remains high in the microchannel centre but not as high as in the water plug centre. When moving towards the microchannel's sidewall (along the z-axis), the velocity magnitude gradually decreases, becoming very small in the liquid film region, at the vicinity of the wall.

As we approach the microchannel's top wall (2y/W=0.8), the velocity magnitude continues to decrease, with a region of lower velocity located in the liquid film zone. This low-velocity region corresponds to the gutters (the corners of the microchannel), as shown in Fig. 31.

For the streamline contour, we can see that the streamlines are oriented towards the microchannel centre once they pass the plug's rear interface, and then they return to the near-wall region once they pass the front interface.

We can also identify a small vortex forming close to the plug tail (2y/W=0), whose size increases as the liquid film thickness increases (increasing the backflow zone) at 2y/w=0.4 and 2y/W=0.8.

The velocity magnitude contours in the YZ plane and along the x-axis for the T-junction and patching methods are shown in Fig. 31. We selected three cross-sections within the water plug and a single cross-section before and after the water plug.

Figure 31 confirms the observations made earlier in Figs. 27 and 30. Within the plug, we can see that the highest velocity is not at the plug centre (along the x-axis) but occurs before reaching the centre. As we progress through the plug, the velocity magnitude gradually decreases until it reaches a low value at the plug head.

We can also see the presence of a low velocity magnitude in the microchannel corners compared to the

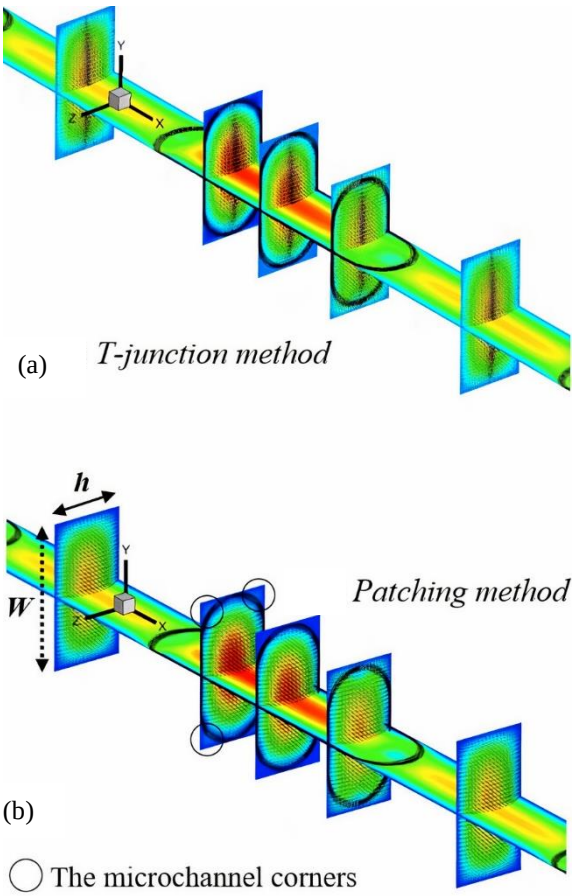

Fig. 31 Contours of velocity magnitude on the YZ plane in and around the water plug along the x-axis for both T-junction and patching methods (EG/W case)

near wall zone in the slug region (continuous phase region). This low fluid velocity in the corner regions can act as an insulator, preventing the water plug from extracting heat properly (Eain et al., 2015).

Figure 32 shows the u(z) velocity profiles for the EG/W case obtained from the T-junction and the patching methods. The profiles are presented in the same XZ planes discussed previously in Fig. 30 (2y/W=0, 2y/W=0.4, and 2y/W=0.8), in five different x-sections before and after the water plug.

Figure 33 illustrates the positions of the selected x-sections. A distance of 0.88W separates sections 1 and 5 from the plug interface, while a distance of 0.42W separates sections 2 and 4 from the water plug.

The velocity profiles have a parabolic shape regardless of the position and method chosen, with a peak velocity located at the microchannel centre (z/h=0). It is apparent from comparing sections 1 and 5 that the velocity profiles are similar, reflecting the periodic nature of the fluid flow.

Moving along the y-axis (from 2y/W=0 to 2y/W=0.4), the *u*-velocity intensity decreases slightly for all the x-sections considered, with a maximum remaining in the microchannel centre (z/h=0). However, when moving from 2y/W=0.4 to 2y/W=0.8, the *u*-velocity decreases significantly, indicating that the microchannel walls (top and bottom wall) are getting closer.

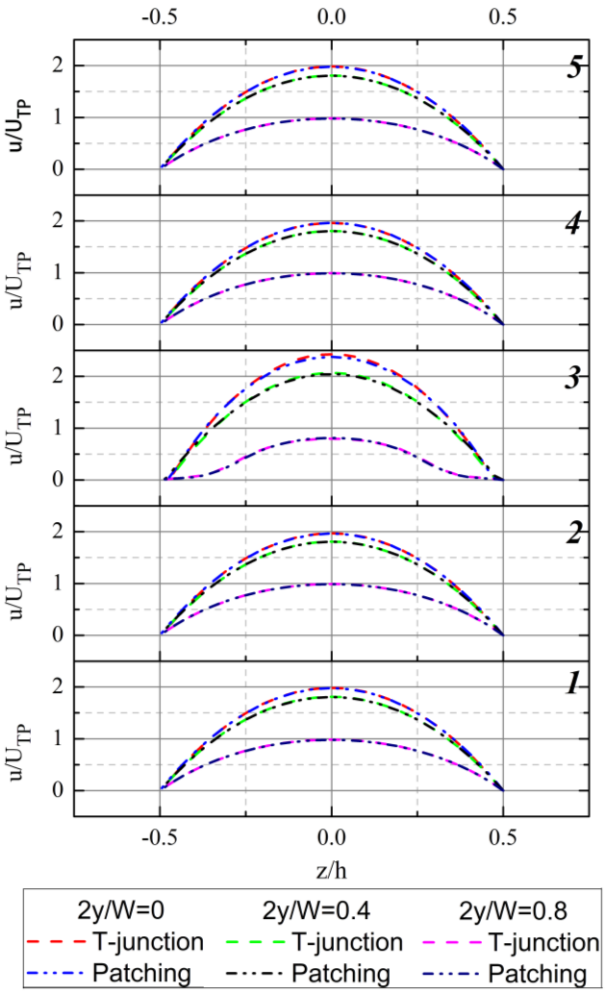

Fig. 32 Velocity profiles *u(z)* at various positions before and after the water plug for both methods (EG/W case)

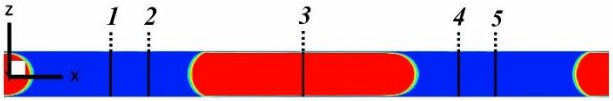

Fig. 33 The selected location for collecting the *u(z)* velocity profiles

5. CONCLUSION

We conducted a comparative study between two numerical methods for generating droplets/plugs (T-junction and patching method). Both methods were examined in a rectangular microchannel (D_h=400 µm), with water droplets dispersed in an ethylene/propylene glycol carrier phase. The comparative study focused on the droplet/plug generation mechanism, liquid film thickness, and plug shape.

A refined mesh near the wall region was required to capture the liquid film separating the dispersed phase from the channel wall. Additionally, a symmetry assumption was considered in each geometry to reduce computational time.

- In the T-junction method, two main stages are identified for plug generation in the transition regime, namely the filling stage and the squeezing stage.
- It was noticed that the filling time was independent of the viscosity ratio λ and capillary number, in agreement with the previous findings of Nekouei and Vanapalli (2017). However, for different flow rate ratios *q*, a slight variation was observed.
- On the other hand, our results for squeezing time indicate a significant influence of the flow rate ratio *q* over the viscosity ratio λ and the Ca number (Ca_{TP}).
- In the patching method, droplets were formed by marking a region close to the channel entrance. Due to droplet development at the corners and in the liquid film area, the final droplet size L_D is usually longer than the initial patch size L_0.
- The patching method was validated by comparing the liquid film results (δ_y and δ_{Cr}) against the experimental correlations reported in the literature and against our previous results (Said et al., 2023).
- To date, no correlation exists for predicting the liquid film thickness δ_y for liquid-liquid systems in rectangular microchannels with low viscosity ratios (*high continuous phase viscosity*).
- Both techniques performed well regarding liquid film ($\delta_{Cr}; \delta_y$) and droplet shape, with only a slight difference between the two methods. However, the patching method was computationally more economical than the T-junction method.

This study would expand and enhance the knowledge about the implementation of numerical methods for droplets hydrodynamics in mini and microchannels.

CONFLICT OF INTEREST

The authors declare that they don't have any conflict of interest.

AUTHORS CONTRIBUTION

Mohammed Said developed the numerical model, conducted the simulations, wrote the manuscript, and prepared all the figures. **N. Nait Bouda** supervised and guided the work with his advice due to his long experience in this field. Finally, **N. Nait Bouda** and **S. Harmand** reviewed and revised the manuscript before submission.

REFERENCES

Abadie, T., Xuereb, C., Legendre, D., & Aubin, J. (2013). Mixing and recirculation characteristics of gas-liquid Taylor flow in microreactors. *Chemical Engineering Research and Design*, *91*(11), 2225–

2234. https://doi.org/10.1016/j.cherd.2013.03.003

Abdollahi, A., Norris, S. E., & Sharma, R. N. (2020). International journal of heat and mass transfer pressure drop and film thickness of liquid-liquid taylor flow in square microchannels. *International Journal of Heat and Mass Transfer*, *156*, 119802. https://doi.org/10.1016/j.ijheatmasstransfer.2020.119802

Bordbar, A., Kamali, R., & Taassob, A. (2018). Thermal Performance Analysis of Slug Flow in Square Microchannels. *Heat Transfer Engineering*, *41*(1), 84-100. https://doi.org/10.1080/01457632.2018.1513630

Asadolahi, A. N., Gupta, R., Fletcher, D. F., & Haynes, B. S. (2011). CFD approaches for the simulation of hydrodynamics and heat transfer in Taylor flow. *Chemical Engineering Science*, *66*(22), 5575–5584. https://doi.org/10.1016/j.ces.2011.07.047

Azarmanesh, M., & Farhadi, M. (2016). The effect of weak-inertia on droplet formation phenomena in T-junction microchannel. *Meccanica*, *51*(4), 819–834. https://doi.org/10.1007/s11012-015-0245-6

Ba, Y., Liu, H., Sun, J., & Zheng, R. (2015). Three dimensional simulations of droplet formation in symmetric and asymmetric T-junctions using the color-gradient lattice Boltzmann model. *International Journal of Heat and Mass Transfer*, *90*, 931–947. https://doi.org/10.1016/j.ijheatmasstransfer.2015.07.023

Bayareh, M., Nasr Esfahany, M., Afshar, N., & Bastegani, M. (2020). Numerical study of slug flow heat transfer in microchannels. *International Journal of Thermal Sciences*, *147*(September 2019), 106118. https://doi.org/10.1016/j.ijthermalsci.2019.106118

Chakraborty, I., Ricouvier, J., Yazhgur, P., Tabeling, P., & Leshansky, A. M. (2019). Droplet generation at Hele-Shaw microfluidic T-junction. *Physics of Fluids*, *31*(2). https://doi.org/10.1063/1.5086808

De menech, M., Garstecki, P., Jousse, F., & Stone, H. A. (2008). Transition from squeezing to dripping in a microfluidic T-shaped junction. *Journal of Fluid Mechanics*, *595*, 141–161. https://doi.org/10.1017/S002211200700910X

Dessimoz, A. L., Cavin, L., Renken, A., & Kiwi-Minsker, L. (2008). Liquid-liquid two-phase flow patterns and mass transfer characteristics in rectangular glass microreactors. *Chemical Engineering Science*, *63*(16), 4035–4044. https://doi.org/10.1016/j.ces.2008.05.005

Dombrowski, N., Foumeny, E. A., Ookawara, S., & Riza, A. (1993). The influence of reynolds number on the entry length and pressure drop for laminar pipe flow. *The Canadian Journal of Chemical Engineering*, *71*(3), 472–476. https://doi.org/10.1002/cjce.5450710320

Garstecki, P., Fuerstman, M. J., Stone, H. A., & Whitesides, G. M. (2006). Formation of droplets and bubbles in a microfluidic T-junction - Scaling and mechanism of break-up. *Lab on a Chip*, *6*(3), 437–446. https://doi.org/10.1039/b510841a

Gupta, R., Fletcher, D. F., & Haynes, B. S. (2009). On the CFD modelling of Taylor flow in microchannels. *Chemical Engineering Science*, *64*(12), 2941–2950. https://doi.org/10.1016/j.ces.2009.03.018

Kashid, M. N., & Renken, A. (2010). Chemical engineering research and design CFD modelling of liquid – liquid multiphase microstructured reactor : Slug flow generation. *Chemical Engineering Research and Design*, *88*(3), 362–368. https://doi.org/10.1016/j.cherd.2009.11.017

Kreutzer, M. T., Kapteijn, F., Moulijn, J. A., & Heiszwolf, J. J. (2005). Multiphase monolith reactors: Chemical reaction engineering of segmented flow in microchannels. *Chemical Engineering Science*, *60*(22), 5895–5916. https://doi.org/10.1016/j.ces.2005.03.022

Li, X. B., Li, F. C., Yang, J. C., Kinoshita, H., Oishi, M., & Oshima, M. (2012). Study on the mechanism of droplet formation in T-junction microchannel. *Chemical Engineering Science*, *69*(1), 340-351. https://doi.org/10.1016/j.ces.2011.10.048

Ma, H., Zhao, Q., Yao, C., Zhao, Y., & Chen, G. (2021). Effect of fluid viscosities on the liquid-liquid slug flow and pressure drop in a rectangular microreactor. *Chemical Engineering Science*, *241*, 116697. https://doi.org/10.1016/j.ces.2021.116697

Eain, M. M. G., Egan, V., & Punch, J. (2013). Film thickness measurements in liquid-liquid slug flow regimes. *International Journal of Heat and Fluid Flow*, *44*, 515–523. https://doi.org/10.1016/j.ijheatfluidflow.2013.08.009

Eain, M. M. G., Egan, V., & Punch, J. (2015). Local Nusselt number enhancements in liquid-liquid Taylor flows. *International Journal of Heat and Mass Transfer*, *80*, 85–97. https://doi.org/10.1016/j.ijheatmasstransfer.2014.09.009

Mehdizadeh, A., Sherif, S. A., & Lear, W. E. (2011). International journal of heat and mass transfer numerical simulation of thermofluid characteristics of two-phase slug flow in microchannels. *International Journal of Heat and Mass Transfer*, *54*(15–16), 3457–3465. https://doi.org/10.1016/j.ijheatmasstransfer.2011.03.040

Navaneetha Krishnan, R., Vivek, S., Chatterjee, D., & Das, S. K. (2010). Performance of numerical schemes in the simulation of two-phase free flows and wall bounded mini channel flows. *Chemical Engineering Science*, *65*(18), 5117–5136. https://doi.org/10.1016/j.ces.2010.06.016

Nekouei, M., & Vanapalli, S. A. (2017). Volume-of-fluid

simulations in microfluidic T-junction devices: Influence of viscosity ratio on droplet size. *Physics of Fluids*, *29*(3). https://doi.org/10.1063/1.4978801

Qian, J., Li, X., Wu, Z., Jin, Z., Zhang, J., & Sunden, B. (2019). Slug formation analysis of liquid–liquid two-phase flow in t-junction microchannels. *Journal of Thermal Science and Engineering Applications*, *11*(5), 1–40. https://doi.org/10.1115/1.4043385

Qin, N., Feng, Y., Wen, J. Z., & Ren, C. L. (2018). Numerical study on single flowing liquid and supercritical CO2 drop in microchannel: Thin film, flow fields, and interfacial profile. *Inventions*, *3*(2). https://doi.org/10.3390/inventions3020035

Said, M., Nait Bouda, N., & Harmand, S. (2023). Numerical investigation of flow patterns and plug hydrodynamics in a 3D T-junction microchannel. *Microgravity Science and Technology*, *35*(1), 8. https://doi.org/10.1007/s12217-022-10026-9

Silva, M. C. F., Campos, J. B. L. M., Miranda, J. M., & Araújo, J. D. P. (2020). Numerical study of single taylor bubble movement through a microchannel using different CFD packages. *Processes*, *8*(11), 1–19. https://doi.org/10.3390/pr8111418

Talimi, V., Muzychka, Y. S., & Kocabiyik, S. (2012). International journal of multiphase flow a review on numerical studies of slug flow hydrodynamics and heat transfer in microtubes and microchannels. *International Journal of Multiphase Flow*, *39*, 88–104. https://doi.org/10.1016/j.ijmultiphaseflow.2011.10.005

Thorsen, T., Roberts, R. W., Arnold, F. H., & Quake, S. R. (2001). *Dynamic pattern formation in a vesicle-generating microfluidic device*. 4163–4166. https://doi.org/10.1103/PhysRevLett.86.4163

Tice, J. D., Lyon, A. D., & Ismagilov, R. F. (2004). Effects of viscosity on droplet formation and mixing in microfluidic channels. *Analytica Chimica Acta*, *507*(1), 73–77. https://doi.org/10.1016/j.aca.2003.11.024

Van Steijn, V., Kreutzer, M. T., & Kleijn, C. R. (2007). μ-PIV study of the formation of segmented flow in microfluidic T-junctions. *Chemical Engineering Science*, *62*(24), 7505–7514. https://doi.org/10.1016/j.ces.2007.08.068

Wang, C., Tian, M., Zhang, J., & Zhang, G. (2021). Experimental study on liquid–liquid two-phase flow patterns and plug hydrodynamics in a small channel. *Experimental Thermal and Fluid Science*, *129*(June), 110455. https://doi.org/10.1016/j.expthermflusci.2021.110455

Wong, V. L., Loizou, K., Lau, P. L., Graham, R. S., & Hewakandamby, B. N. (2017). Numerical studies of shear-thinning droplet formation in a microfluidic T-junction using two-phase level-SET method. *Chemical Engineering Science*, *174*, 157–173. https://doi.org/10.1016/j.ces.2017.08.027

Yan, Y., Guo, D., & Wen, S. Z. (2012). Numerical simulation of junction point pressure during droplet formation in a microfluidic T-junction. *Chemical Engineering Science*, *84*, 591–601. https://doi.org/10.1016/j.ces.2012.08.055

Yao, C., Zheng, J., Zhao, Y., Zhang, Q., & Chen, G. (2019). Characteristics of gas-liquid Taylor flow with different liquid viscosities in a rectangular microchannel. *Chemical Engineering Journal*, *373*(May), 437–445. *https://doi.org/10.1016/j.cej.2019.05.051*

Zhou, C. H., & Ai, J. Q. (2013). Mesh adaptation for simulation of unsteady flow with moving immersed boundaries. *International Journal for Numerical Methods in Fluids* *72*(4) 453–477. https://doi.org/10.1002/fld.3751